Quantum information scrambling in the presence of weak and strong thermalization

Zheng-Hang Sun,[1,2] Jian Cui,[3,*] and Heng Fan[1,2,4,†]
[1]*Institute of Physics, Chinese Academy of Sciences, Beijing 100190, China*
[2]*School of Physical Sciences, University of Chinese Academy of Sciences, Beijing 100190, China*
[3]*School of Physics, Beihang University, Beijing 100191, China*
[4]*Songshan Lake Materials Laboratory, Dongguan 523808, Guangdong, China*

(Received 28 December 2020; revised 5 July 2021; accepted 14 July 2021; published 5 August 2021)

Quantum information scrambling under the dynamics of a closed many-body system is of wide interest. The tripartite mutual information (TMI) can quantify the scrambling via its stable negative value under temporal evolution. Here, we study the quench dynamics of the TMI in a nonintegrable Ising model with different initial states in the regimes of strong and weak thermalization. Our numerical results show that the most efficient scrambling can occur when the inverse temperatures of initial states are near zero and in the regime of strong thermalization, and weak thermalization accompanies slow scrambling. We then present an experimental protocol for observing strong and weak thermalization in a one-dimensional array of superconducting qubits, based on which the relation between scrambling and the degree of thermalization revealed in this work can be directly verified by superconducting quantum simulators. The inevitable decoherence effects in real situations are also analyzed, paving the way for faithful quantum simulations on actual experimental platforms.

DOI: 10.1103/PhysRevA.104.022405

I. INTRODUCTION

Under unitary dynamics, whether or not the locally encoded quantum information is localized or spreads over the entire system is a fundamental question [1,2]. When delocalization of quantum information occurs in a system, it is referred to as a scrambler. For instance, the most efficient scrambler in nature is the black hole [3–5]. The characterization of scramblers has attracted considerable attention [6–9]. A well-known probe of quantum information scrambling is the out-of-time-order correlator (OTOC), whose decay rate extracted from its dynamics is closely related to the Lyapunov exponent [6,10]. Quantum information scrambling can provide insight into the subjects in condensed-matter physics. By studying OTOCs, it has been recognized that the scrambling plays an important role in information propagation [11,12], many-body localization (MBL) transitions [13–15], and quantum phase transitions [16–19].

Besides the OTOC, the scrambling can also be characterized by the negative tripartite mutual information (TMI) [6,7]. Different from the OTOC, the TMI is an operator-independent quantity. The experimental measurements of OTOCs and TMI require different technologies. The direct measurement of OTOCs requires the inverse-time evolution, which can be performed in trapped ions [20] and nuclear magnetic resonance (NMR) quantum simulators [21]. Nevertheless, the inverse-time evolution is an experimental challenge in superconducting circuits because the sign of local intraqubit interactions cannot be adjusted on the fly [22]. On the other hand, measuring the TMI calls for quantum state tomography (QST). Accurate and efficient QST can be performed in several platforms, such as trapped ions [23], superconducting qubits [22,24,25], and NMR [26]. Consequently, TMI is an experimentally feasible probe for quantum information scrambling in general.

Recently, more attention has been paid to the TMI in quantum many-body systems. It has been shown that the TMI can diagnose the ergodic and the MBL phase; i.e., the TMI is close to zero and the scrambling is suppressed in the MBL phase. In contrast, the TMI becomes more negative in the ergodic phase, indicating stronger scrambling [27]. In addition, by studying the TMI, it has been shown that the scrambling is observed in both the Bethe integrable system with fermionic interactions and a generic nonintegrable system, while one-dimensional noninteracting fermions do not scramble [28].

Quantum information scrambling accompanies thermalization in quantum many-body systems driven out of equilibrium. If thermalization occurs, the dynamics of local observables will stably attain their thermal values predicted by the Gibbs ensemble. The occurrence of the aforementioned thermalization (known as strong thermalization) is dependent on the choice of initial states. Starting from an initial state corresponding to the Gibbs state with an inverse temperature β far away from zero, it has been revealed that the dynamics of local observables shows obvious persistent oscillation, and can achieve the thermal values only by adopting the long-time average, which is a signature of weak thermalization. In contrast, strong thermalization happens when the inverse temperatures of initial states are close to zero. The weak and strong thermalization in a nonintegrable Ising model with both parallel and longitude magnetic fields was numerically explored [29,30], and explained from a quasiparticle viewpoint [31]. Recent numerical results of

*jianCui@buaa.edu.cn
†hfan@iphy.ac.cn

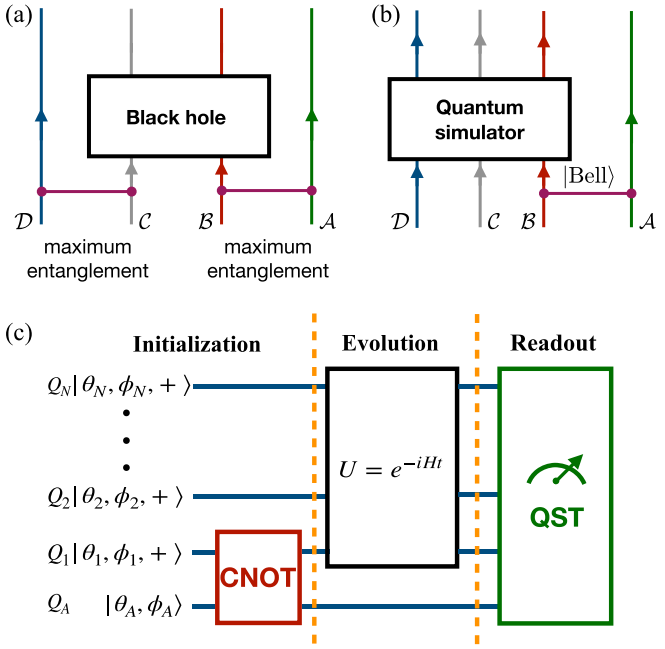

FIG. 1. (a) Schematic representation of the Hayden-Preskill thought experiment. (b) A protocol for characterizing information scrambling in the quantum simulator enlightened by the Hayden-Preskill thought experiment. The arrows in (a) and (b) represent the direction of time. (c) Schematic representation of the generic experimental protocol for studying quantum information scrambling by measuring the TMI. The sequence consists of three parts: (i) initialization, (ii) evolution, and (iii) readout. Throughout the protocol, the whole system remains in a pure state.

the nonintegrable long-range Ising model suggest the existence of strong and weak thermalization in this system, paving the way to experimentally observing the phenomena in trapped ions [32].

Previous works of the TMI mainly focused on whether the integrability of the system is broken. However, its dependence on the initial states with different temperatures in nonintegrable systems remains limited. In this work, we first study the time evolution of TMI in the nonintegrable Ising model with different initial states in the regimes of both strong and weak thermalization, and reveal the relation between the information scrambling and the degree of thermalization. We then present an experimental protocol for observing weak and strong thermalization in a superconducting qubit chain, which constitutes one of the most common superconducting circuits. Finally, we calculate the TMI in the superconducting qubit chain and explore the impact of decoherence on the TMI.

II. TRIPARTITE MUTUAL INFORMATION AND A GENERIC EXPERIMENTAL PROTOCOL

We first introduce the Hayden-Preskill thought experiment [3] [see Fig. 1(a)], which can be further employed to quantify the information scrambling [27]. Four parties are involved in the thought experiment: Party $\mathcal{B}$ holds certain quantum information encoded in its state. Party $\mathcal{A}$ is an ancillary system acting as a reference, which is maximally entangled with $\mathcal{B}$, so that $\mathcal{B}$'s information can be reflected by $\mathcal{A}$ through the entanglement between them. Party $\mathcal{C}$, being the black hole, is the information scrambler, and party $\mathcal{D}$ is an examiner of $\mathcal{C}$, if needed. The powerful examiner $\mathcal{D}$ has full knowledge of $\mathcal{C}$ by maximally entangling with it. In this setup, $\mathcal{B}$ wants to hide and erase its quantum information through the scrambler $\mathcal{C}$ by throwing its physical qubits into the black hole and letting them interact. There, one is interested in how it is possible for party $\mathcal{D}$ to retrieve the information of party $\mathcal{B}$ by collecting the Hawking radiation of the evaporating black hole and selecting part of his qubits such that they are also maximally entangled with the reference system $\mathcal{A}$. One key ingredient as such is the ability of the black hole to efficiently scramble information.

Now, we consider a more realistic scenario of using a quantum simulator as an information scrambler, where the whole system, consisting of $\mathcal{A}$, $\mathcal{B}$, $\mathcal{C}$, and $\mathcal{D}$, is always a pure state. Similar to the black hole setup, the ancillary reference system $\mathcal{A}$ will not participate in the unitary transformation after getting maximally entangled with $\mathcal{B}$. Unlike the black hole scenario, where nobody is able to directly detect the black hole, and as a result one has to employ an examiner $\mathcal{D}$ which is maximally entangled with $\mathcal{C}$, in our case, there is no need to include the examiner $\mathcal{D}$, since the quantum simulator can be directly detected. However, to keep the discussion consistent with the Hayden-Preskill thought experiment, we preserve the party $\mathcal{D}$, which is initially independent of $\mathcal{C}$, but under the dynamics of the quantum simulator together with $\mathcal{C}$ [see Fig. 1(b)].

In the Hayden-Preskill thought experiment [3], the system size of $\mathcal{A}$ is exactly equal to that of $\mathcal{B}$, and $\mathcal{D}$ should be comparable with $\mathcal{C}$. Moreover, the former two subsystems should be much smaller than the latter two in order for $\mathcal{C}$ to sufficiently and efficiently scramble the quantum information of $\mathcal{B}$. Here, we focus on a simple situation where $\mathcal{A}$ and $\mathcal{B}$ each only have one qubit.

The reduced density matrices of the subsystems $\mathcal{A}$, $\mathcal{B}$, $\mathcal{C}$, and $\mathcal{D}$ are denoted as $\rho_{\mathcal{A}}$, $\rho_{\mathcal{B}}$, $\rho_{\mathcal{C}}$, and $\rho_{\mathcal{D}}$, respectively. In general, the definition of TMI is [6]

$$I_3 = S(\rho_{\mathcal{A}}) + S(\rho_{\mathcal{B}}) + S(\rho_{\mathcal{C}}) + S(\rho_{\mathcal{D}}) - S(\rho_{\mathcal{AB}}) - S(\rho_{\mathcal{AC}}) - S(\rho_{\mathcal{BC}}), \quad (1)$$

where $S(\rho) = -\mathrm{Tr}(\rho \ln \rho)$ is the von Neumann entanglement entropy (EE). A stable negative value obviously away from zero is a diagnostic of quantum information scrambling [6].

We then present a generic experimental protocol for studying quantum information scrambling by measuring the TMI. A schematic diagram of the protocol is shown in Fig. 1(c). The whole system is comprised of N qubits denoted as $Q_1, Q_2, \ldots, Q_N$, and an ancillary qubit Q_A. They are assigned to four parties as $Q_A \in \mathcal{A}$, $Q_1 \in \mathcal{B}$, $\{Q_2, \ldots, Q_i\} \in \mathcal{C}$, and $\{Q_{i+1}, \ldots, Q_N\} \in \mathcal{D}$. We define the state $|\theta, \phi, \pm\rangle$ as the eigenstate of the matrix $\hat{n} \cdot \vec{\sigma} = (\sin\theta\cos\phi)\sigma^x + (\sin\theta\sin\phi)\sigma^y + (\cos\theta)\sigma^z$ (σ^α with $\alpha \in \{x, y, z\}$ referring to the Pauli matrices) with the eigenvalues ± 1. The initial state of Q_A is $|\theta_A, \phi_A\rangle \equiv (|\theta_1, \phi_1, +\rangle + |\theta_1, \phi_1, -\rangle)/\sqrt{2}$, and all other qubits are in $|\theta_1, \phi_1, +\rangle$. The generalized controlled-NOT

(CNOT) gate in Fig. 1(c) reads

$$\begin{aligned}\text{CNOT} \equiv\ & |\theta_1, \phi_1, +\rangle\langle\theta_1, \phi_1, +| \otimes \mathbf{1} \\ & + |\theta_1, \phi_1, -\rangle\langle\theta_1, \phi_1, -| \otimes \tilde{X},\end{aligned} \tag{2}$$

where $\mathbf{1}$ is a two-dimensional identity matrix, and $\tilde{X} \equiv R\sigma^x R^{-1}$ with

$$R \equiv \begin{pmatrix} \cos\frac{\theta_1}{2} & -e^{-i\phi_1}\sin\frac{\theta_1}{2} \\ e^{i\phi_1}\sin\frac{\theta_1}{2} & \cos\frac{\theta_1}{2} \end{pmatrix}. \tag{3}$$

After applying the CNOT gate, we in fact generate a Bell state $|\Phi\rangle_{A1} = (|\theta_1, \phi_1, +\rangle_A|\theta_1, \phi_1, +\rangle_1 + |\theta_1, \phi_1, -\rangle_A|\theta_1, \phi_1, -\rangle_1)/\sqrt{2}$, maximally entangling the ancillary qubit and Q_1 and locally encoding the information in the two qubits [see Figs. 1(b) and 1(c)]. In short, the initial state can be written as

$$|\psi_0\rangle = |\Phi\rangle_{A1}(\otimes_{j=2}^{N}|\theta_j, \phi_j, +\rangle). \tag{4}$$

The next step is the time evolution under the quantum channel $U = e^{-iHt}$, i.e., $|\psi_t\rangle = U|\psi_0\rangle$, with H as the Hamiltonian of the N-qubit isolated system. To study the quantum information scrambling, we conventionally consider the spin chains that are beyond quadratic fermionic form after the Jordan-Wigner transformation [28]. The final step is measuring the TMI by QST based on Eq. (1). In this work, we adopt the open boundary condition for the physical systems studied below.

III. RESULTS

A. Results for a nonintegrable Ising model

We first pay attention to a spin-1/2 Ising model whose Hamiltonian reads

$$H_{\text{Ising}} = -J\sum_{i=1}^{N-1}\sigma_i^z\sigma_{i+1}^z + g\sum_{i=1}^{N}\sigma_i^x + h\sum_{i=1}^{N}\sigma_i^z, \tag{5}$$

with g and h referring to the strength of the transverse and the parallel magnetic fields. With the chosen parameters $g/J = 1.05$ and $h/J = -0.5$, the Ising model becomes a paradigmatic nonintegrable model [29–31]. Similar to the quench protocol in Ref. [29], the chosen initial states are isotropic, i.e., $\theta = \theta_i$ and $\phi = \phi_i$ $\forall i \in \{1, 2, \ldots, N\}$ in Eq. (4), and $|\theta, \phi\rangle \equiv \otimes_{i=1}^{N}|\theta_i, \phi_i, +\rangle$. The inverse temperature β for the state $|\theta, \phi\rangle$ can be obtained by solving the equation $\text{Tr}\{[\rho(\beta) - \rho(\theta, \phi)]H\} = 0$ with $\rho(\theta, \phi) \equiv |\theta, \phi\rangle\langle\theta, \phi|$, $\rho(\beta) \equiv e^{-\beta H}/\text{Tr}(e^{-\beta H})$, and H as the Hamiltonian.

It has been shown that the quench dynamics with the initial state $|Z+\rangle = |0, \phi, +\rangle$ (i.e., $\beta \simeq 0.7275$) shows a signature of weak thermalization, while with $|Y+\rangle = |\pi/2, \pi/2, +\rangle$ (i.e., $\beta = 0$) as the initial state, strong thermalization occurs [29]. Additionally, we can employ the normalized energy

$$\epsilon = \frac{\langle\theta, \phi, +|H|\theta, \phi, +\rangle - E_{\text{min}}}{E_{\text{max}} - E_{\text{min}}} \tag{6}$$

with $E_{\text{max(min)}}$ as the maximum (minimum) eigenvalue of the Hamiltonian H. The normalized energy can quantify the relative position of the state in the energy spectrum. It can be directly calculated that for $|Z+\rangle$ in the weak thermalization regime, the normalized energy $\epsilon \simeq 0.0812$, i.e., $|Z+\rangle$ is quite close to the ground state of H_{Ising} (here, the system size is $N = 14$), which is consistent with the quasiparticle explanation in Ref. [31]. For the state $|Y+\rangle$, which is far away from the ground state, the normalized energy is $\epsilon \simeq 0.5602$.

Using the protocol in Fig. 1, we study the quench dynamics of TMI I_3 in the nonintegrable Ising model with the Hamiltonian (5). We first explore the dependence of I_3 on the length of subsystem $\mathcal{C}$ denoted as l. Considering different l, the time evolution of I_3 with the initial state $|Y+\rangle$ and $|Z+\rangle$ is displayed in Figs. 2(a) and 2(b), respectively. It is shown that except for $l = 6$ and 7, the I_3 tends to a value close to zero for both strong ($|Y+\rangle$) and weak ($|Z+\rangle$) thermalization. The values of I_3 at late time for weak and strong thermalization are the most distinctive when $l = 6$ and 7. We also consider a time-averaged TMI $\overline{I_3} \equiv \frac{1}{t_f - t_i}\int_{t_i}^{t_f} I_3(t)\,dt$ with $t_i = 100$ and $t_f = 1000$, extracting the stationary value of TMI from its dynamics. The $\overline{I_3}$ as a function of l is plotted in Fig. 2(c), suggesting that to characterize the regimes of strong and weak thermalization using the dynamics of I_3, the appropriate length of subsystem $\mathcal{C}$ is $l = N/2 - 1$ or $N/2$ (N is even for convenience). Consequently, we fix $l = 6$, i.e., the subsystem $\mathcal{C} = \{Q_2, Q_3, \ldots, Q_7\}$ for a 14-qubit system in the following studies.

As shown in Fig. 2(d), when ϕ varies from zero to 0.5π with $\theta = 0.5\pi$, the decrease of TMI suggests that stronger thermalization corresponds to more efficient information scrambling. The dynamics of I_3 with $\phi = 0.5\pi$ and $\theta \in [0, 0.5\pi]$ is presented in Fig. 2(e), showing a similar tendency of TMI in Fig. 2(d). The normalized energy ϵ can characterize the initial states in the strong or weak thermalization regime, and therefore we plot the $\overline{I_3}$ as a function of ϵ in Fig. 2(f). The $\overline{I_3}$ has a local minimum value near $\epsilon \simeq 0.56$, which exactly corresponds to a maximum density of states (DOS) (see Appendix A), revealing that the most efficient scrambling occurs when the initial state has the normalized energy with maximal DOS, equivalent to the inverse temperature $\beta = 0$.

As a side remark, we compare the dynamics of TMI for different isotropic initial states and the initial Néel-type initial states with the same ϵ. The results are presented in Appendix A, showing that the stationary values of TMI are almost identical for all initial states with the same ϵ.

B. Experimental protocol for observing weak and strong thermalization on a superconducting qubit chain

In the above section, we have studied the relation between the information scrambling quantified by the TMI and the degree of thermalization characterized by initial states with different normalized energy or temperature in the nonintegrable Ising model [Eq. (5)]. To experimentally demonstrate the relation in the Ising model using superconducting qubits, one can employ the digital quantum simulation to realize the Ising interaction [33,34], which cannot be directly realized in the setup, since a chain of transmon qubits with capacitive couplings λ is typically described by the one-dimensional (1D) spin-1/2 XY model [22,35–37]

$$H_{XY} = \lambda\sum_{i=1}^{N-1}\left(\sigma_i^x\sigma_{i+1}^x + \sigma_i^y\sigma_{i+1}^y\right). \tag{7}$$

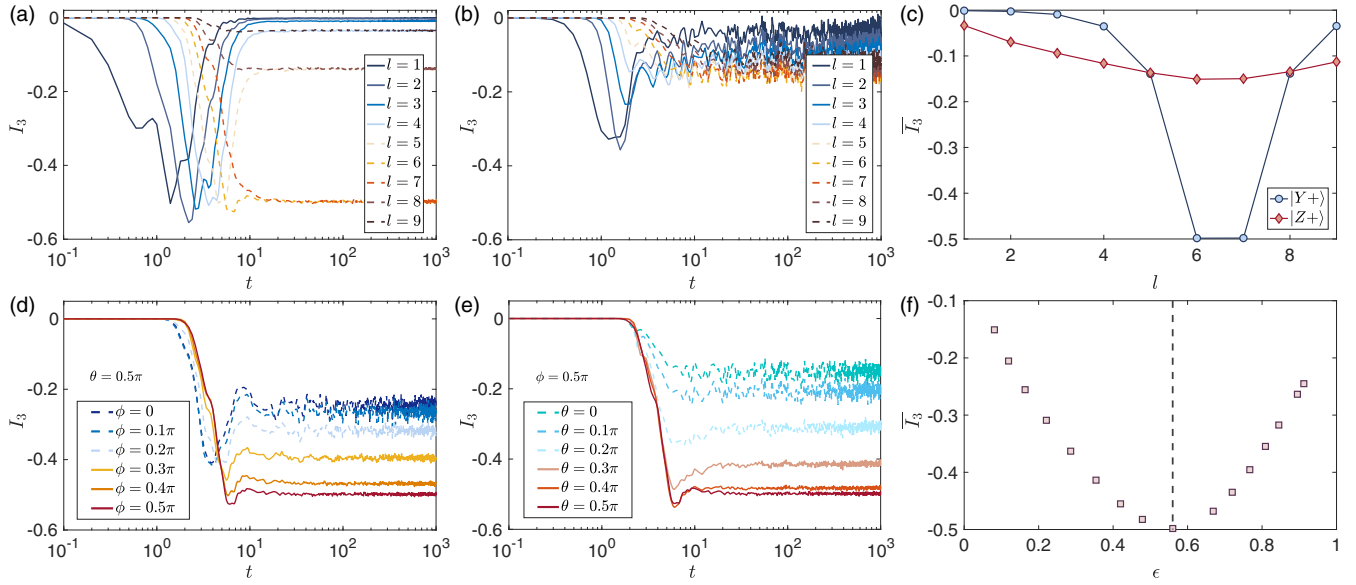

FIG. 2. (a) Time evolution of the TMI I_3 in the nonintegrable Ising model [Eq. (5)] with $g/J = 1.05$, $h/J = -0.5$, system size $N = 14$, and different length of the subsystem $\mathcal{C}$, i.e., l. The initial state is chosen as $|Y+\rangle$. (b) Similar to (a) but for the initial state $|Z+\rangle$. (c) The time-averaged TMI $\overline{I_3}$ as a function of l with two initial states $|Y+\rangle$ and $|Z+\rangle$. (d, e) The dynamics of the I_3 with $l = 6$ and different isotropic initial states $|\theta, \phi\rangle$. (f) The $\overline{I_3}$ as a function of the normalized energy ϵ with $l = 6$. The dashed line in (f) highlights the ϵ corresponding to the minimum $\overline{I_3}$. The unit of time t is $1/J$.

It has been revealed that the Trotter error in the digital quantum simulation of the Ising model is proportional to the number of qubits, N [33], bringing the experimental challenge to the implementation of the nonintegrable Ising model [Eq. (5)] with large size in superconducting qubits.

Nevertheless, the phenomena of strong and weak thermalization do not uniquely exhibit in the Hamiltonian in Eq. (5). Actually, any nonintegrable model is a potential platform to observe strong and weak thermalization, for instance, the long-range transverse-field Ising model studied in Ref. [32]. Thus, in the following, we construct a nonintegrable model using a 1D array of transmon qubits, and present a protocol of *analog* quantum simulation to study strong and weak thermalization, as well as the dynamics of TMI in different regimes of thermalization.

The Hamiltonian H_{XY} can be mapped to a free fermion system via the Jordan-Wigner transformation [38]. Thus, quantum thermalization is absent in H_{XY} because of the infinitely many conserved quantities in the thermodynamic limit (for a finite XY chain, there are an extensive number of conserved quantities) [39,40]. To make the superconducting qubit chain nonintegrable for observing quantum thermalization, we impose uniform resonant microwave drives on all qubits, generating the local transverse field with amplitude Ω, and the final Hamiltonian reads (see Appendix B)

$$H_{\mathrm{SQ}} = \lambda \sum_{i=1}^{N-1} \left(\sigma_i^x \sigma_{i+1}^x + \sigma_i^y \sigma_{i+1}^y\right) + \Omega \sum_{i=1}^{N} \sigma_i^y. \tag{8}$$

The local transverse field has been realized in a recent quantum simulation experiment [41], where the XY-crosstalk correction and phase alignment of the transverse field were discussed. A sketch of the pulse sequence for the realization of the Hamiltonian (8) is depicted in Fig. 3. More details for the breakdown of integrability in Eq. (7) due to the term $\Omega \sum_{i=1}^{N} \sigma_i^y$ are presented in Appendix B.

Before we study the TMI in Hamiltonian (8), weak and strong thermalization in the system should be demonstrated. Here, we adopt $\lambda = \Omega = 1$ and $N = 14$. It can be

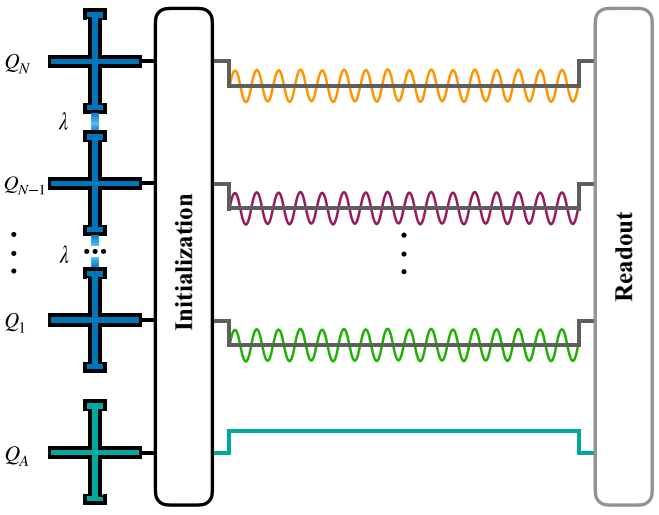

FIG. 3. Schematic representation of the experimental waveform sequence for the time evolution. The qubits $Q_1, Q_2, \ldots, Q_N$ are biased to the interaction frequency ω_q^{int} via their Z pulse control lines (the rectangular pulses). Since the ancillary qubit Q_A does not participate in the time evolution, its frequency should be detuned away from ω_q^{int}. Meanwhile, the microwave drives (the sinusoidal pulses) are imposed on $Q_1, Q_2, \ldots, Q_N$ through the XY control lines.

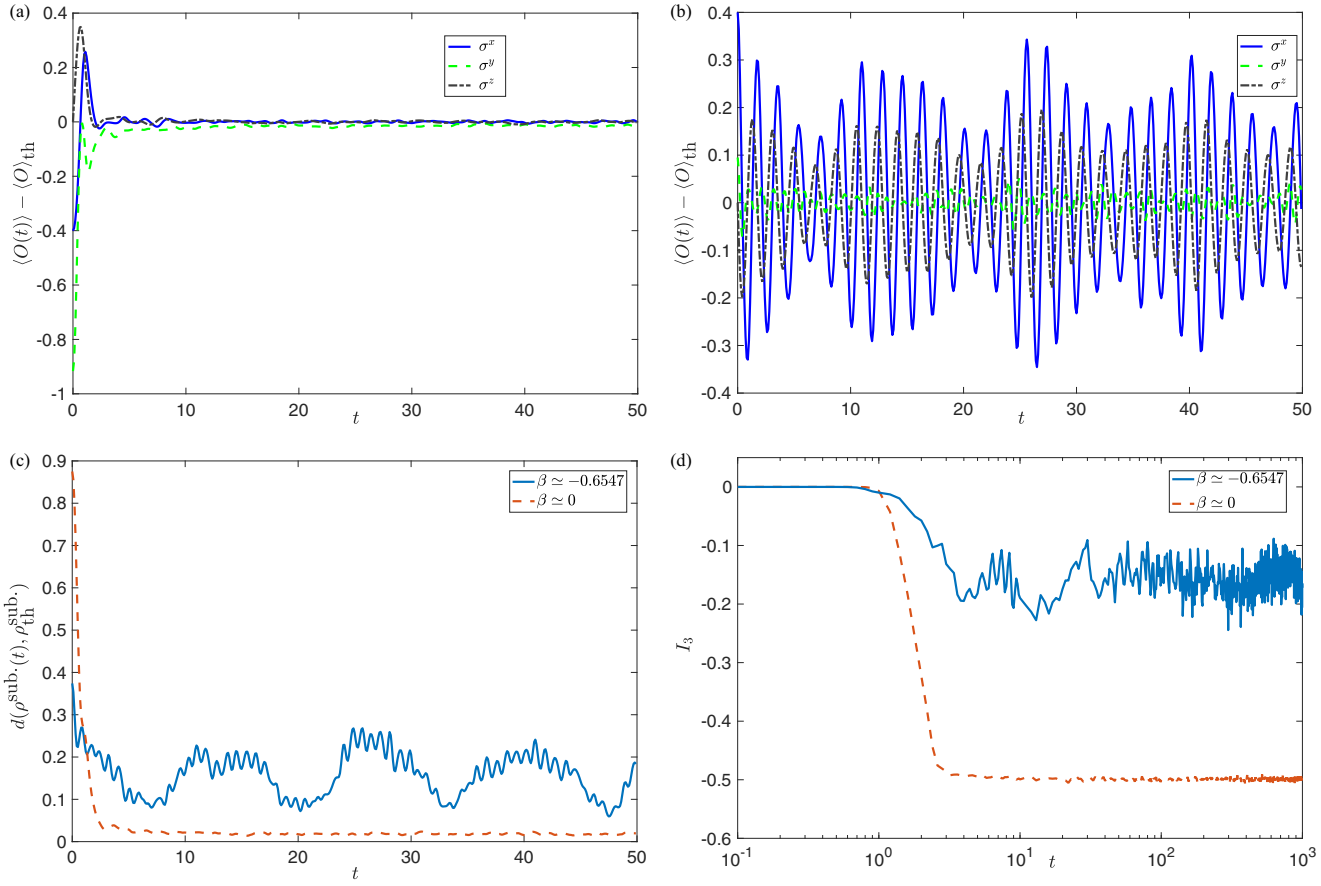

FIG. 4. (a) The dynamics of local observables with the initial state $|\theta, \phi\rangle = |\pi/2, 1.369\pi\rangle$ ($\beta \simeq 0$) for the superconducting circuit model [Eq. (8)] with $\lambda = \Omega = 1$, and system size $N = 14$. (b) Similar to (a) but with the initial state $|\theta, \phi\rangle = |\pi/2, 0.369\pi\rangle$ ($\beta \simeq -0.6547$). (c) Time evolution of the distance $d(\rho^{\rm sub.}(t), \rho^{\rm sub.}_{\rm th})$ with the two initial states. (d) Similar to (c) but for the dynamics of TMI. The unit of time t is $1/\lambda$.

calculated that for the isotropic initial state $|\theta, \phi\rangle = |\pi/2, 1.369\pi\rangle$, the inverse temperature $\beta \simeq 0$, and strong thermalization is expected. To observe the weak thermalization, we consider another isotropic initial state $|\pi/2, 0.369\pi\rangle$ with $\beta \simeq -0.6547$.

To characterize strong and weak thermalization, we study the quench dynamics of local observables $\langle O(t)\rangle - \langle O\rangle_{\rm th}$ with $O \in \{\sigma^x, \sigma^y, \sigma^z\}$, and the operator norm distance between a reduced density matrix (RDM) of a three-body subsystem and the corresponding thermal density matrix, i.e., $d(\rho^{\rm sub.}(t), \rho^{\rm sub.}_{\rm th})$ defined as the maximum eigenvalue of the matrix $\rho^{\rm sub.}(t) - \rho^{\rm sub.}_{\rm th}$. Here we chose the subsystem consisting of the qubits Q_5, Q_6, and Q_7. The time evolution of local observables with two different initial states is shown in Figs. 4(a) and 4(b). One can see that the observables relax to the thermal values when the initial state is $|\theta, \phi\rangle = |\pi/2, 1.369\pi\rangle$ ($\beta \simeq 0$) in the strong-thermalization regime. However, the undamped oscillation of $\langle O(t)\rangle - \langle O\rangle_{\rm th}$ can be observed with another initial state $|\theta, \phi\rangle = |\pi/2, 0.369\pi\rangle$, which is a signature of the weak thermalization. Moreover, the dynamics of $d(\rho^{\rm sub.}(t), \rho^{\rm sub.}_{\rm th})$ with the two initial states is shown in Fig. 4(c). In the strong-thermalization region, the quenched RDM quickly saturates to the thermal state and the distance $d(\rho^{\rm sub.}(t), \rho^{\rm sub.}_{\rm th})$ monotonically decays, while the distance exhibits dramatic fluctuation in the weak-thermalization regime.

C. Results for the superconducting qubit chain

We then study the TMI I_3 in Hamiltonian (8). The time evolution of I_3 with various initial states is presented in Fig. 4(d). The behaviors of I_3 are similar to those in the nonintegrable Ising model [see Figs. 2(d) and 2(e)]. Efficient and slow quantum information scrambling are observed in the strong- and weak-thermalization regions, respectively. Moreover, the saturation of I_3 at long time can also be observed in system (8).

Next, we study the relation between the TMI and the normalized energy ϵ. Different from the Ising model [Eq. (5)], the minimum attainable ϵ of all isotropic states is 0.3093 in system (8) (see Appendix A). To study the I_3 of the initial states with $\epsilon < 0.3093$, we can consider the Néel-type initial states (see Appendix A). The time-averaged TMI $\overline{I_3} \equiv \frac{1}{t_f - t_i}\int_{t_i}^{t_f} I_3(t)dt$ ($t_i = 100$ and $t_f = 1000$) as a function of ϵ is displayed in Fig. 5. It is shown that the most efficient information scrambling diagnosed by $\overline{I_3} \simeq -0.5$ occurs when the initial state has the normalized energy $\epsilon \simeq 0.39$, accompanying the inverse temperature $\beta \simeq 0$, and the maximum DOS (see Appendix A).

The results of I_3 in Hamiltonian (8) suggest that the linkage between information scrambling and thermalization revealed in the Ising model [Eq. (5)] is not unique to a specific model, and can be experimentally verified in the superconducting

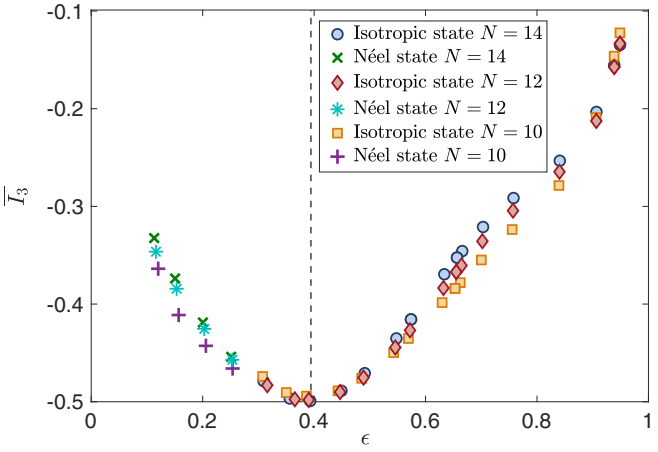

FIG. 5. The time-averaged TMI $\overline{I_3}$ as a function of the normalized energy ϵ for the superconducting circuit model [Eq. (8)] with different system size. The dashed line highlights the ϵ corresponding to the minimum $\overline{I_3}$. For the system with size $N = 12$ and $N = 10$, the length of the subsystem $\mathcal{C}$ is $l = 5$ and 4, respectively.

qubit chain using the protocol. We also note that for both the nonintegrable Ising model (5) and system (8), in the strong-thermalization regime, the TMI approaches -0.5 at long time, which is consistent with the dynamics under a Haar random circuit (see Appendix C).

Here, we note that the universal minimal value of TMI, -0.5, in the regime of strong thermalization and the Haar random circuit come from the Page value, i.e., the average entropy of a subsystem of a random pure state, which is defined as [42]

$$S^{\text{Page}}_{m,n} = \ln(m) - \frac{m}{2n}, \tag{9}$$

where $m = 2^s$ and $n = 2^{\mathcal{N}-s}$ with s and $\mathcal{N}$ being the size of the subsystem and the total system. Considering our protocol in Fig. 1(c) with the total system size $\mathcal{N} = 15$ including an ancillary qubit, $S^{\text{Page}}(\rho_{\mathcal{A}}) = S^{\text{Page}}(\rho_{\mathcal{B}}) = 0.6931$ $(s = 1)$, $S^{\text{Page}}(\rho_{\mathcal{AB}}) = 1.3861$ $(s = 2)$, $S^{\text{Page}}(\rho_{\mathcal{C}}) = 4.0964$ $(s = 6)$, and $S^{\text{Page}}(\rho_{\mathcal{AC}}) = S^{\text{Page}}(\rho_{\mathcal{BC}}) = S^{\text{Page}}(\rho_{\mathcal{D}}) = 4.6020$ $(s = 7)$. Thus, according to Eq. (1), we can directly obtain $I_3^{\text{Page}} \simeq -0.5$.

We further study the time-averaged TMI for initial states with various ϵ in the Hamiltonian H_{SQ} with smaller number of qubits $N = 10$, 12, and the results are depicted in Fig. 5. It is seen that the time-averaged TMI does not suffer from the finite-size effect.

D. The effects of decoherence

The coupling of superconducting qubits to the environment is unavoidable in quantum simulations, which leads to decoherence affecting the dynamics of TMI. Here, we consider both the energy relaxation effect and dephasing effect, quantified by the energy lifetime T_1 and Ramsey dephasing time T_2, respectively.

The dissipative dynamics under Markovian approximation can be numerically simulated by solving the Lindblad master equation [43]

$$\dot{\rho}_t = -i[H, \rho_t] + \frac{1}{2}\sum_n (2L_n\rho_t L_n^\dagger - \{L_n^\dagger L_n, \rho_t\}), \tag{10}$$

where ρ_t is the density matrix of the quenched state, and L_n ($L_n^\dagger$) refers to the Lindblad operators for the Markovian dissipation. For the energy relaxation and dephasing effect, the Lindblad operator is $L_n = \frac{1}{\sqrt{T_1}}\sigma_n^-$ and $L_n = \frac{1}{\sqrt{2T_2}}\sigma_n^z$, respectively. According to recent developments of superconducting qubits, for system (8), the energy lifetime and Ramsey dephasing time are estimated as $T_1 \simeq 800$ and $T_2 \simeq 100$ (in the unit of the hopping interaction $\lambda = 1$) [22].

Below, we will present the dynamics of TMI with different T_1 and T_2. Since the finite-size effect of I_3 is not dramatic (see Fig. 5), we consider Hamiltonian (8) with $N = 10$. As shown in Fig. 6(a), for the initial state $|\pi/2, 1.369\pi\rangle$ in the strong-thermalization regime, the saturation of I_3 under unitary evolution ($T_1 \to \infty$) is destroyed by the decoherence. With the decrease of T_1, the time evolution of I_3 tends to zero. For weak thermalization, i.e., with the initial state $|\pi/2, 0.369\pi\rangle$, the value of I_3 also becomes closer to zero in the presence of shorter T_1 [see Fig. 6(b)]. We also present the results of the dynamics of I_3 with different T_2 in the regimes of strong and weak thermalization in Figs. 6(c) and 6(d), respectively. It is seen that the impact of dephasing on I_3 is similar to that of energy relaxation.

In Fig. 6, one can notice that for the given dissipation rates, the decoherence plays its role only after accumulating its effects for certain duration longer than $t = 10$. Consequently, we can extract the minimum TMI I_3^{min} from its dynamics with the time $t \leqslant 10$. As depicted in Figs. 7(a) and 7(b), although the I_3^{min} sightly decays with the increase of T_1 [see the inset of Fig. 7(a)], the difference between the TMI in the regimes of strong and weak thermalization is still obvious. We then study the I_3^{min} with different normalized energy ϵ around $\epsilon = 0.39$ corresponding to the maximum DOS (see Fig. 5). We consider $T_1 = 500$ and $T_2 = 100$ as the conditions with relatively strong decoherence. As shown in Fig. 7(c), there is a cusp of the I_3^{min} as a function of ϵ, which is consistent with the results in Figs. 2(b) and 5.

E. Physical argument

We have shown that the relation between the value of TMI after a long-time evolution and the normalized energy ϵ of initial states is valid for both the nonintegrable Ising model (5) and the superconducting circuit model (8). To explain the relation, we present additional numerical results in Appendix D, including the EE of the eigenstates of the studied models and the superposition of quenched states. Two remarks are in order. First, the long-time quenched state $|\psi_t\rangle = \exp(-iHt)|\psi_0\rangle$ can be written as the superposition of eigenstates of the Hamiltonian H. It can be demonstrated that the eigenstates near the ϵ of the chosen initial state $|\psi_0\rangle$ have the main contribution to the quenched state $|\psi_t\rangle$. Second, for the half-chain EE of the eigenstates, the EE as a function of the ϵ of eigenstates closely relates to the DOS. In the regime of high DOS, the EE approaches the

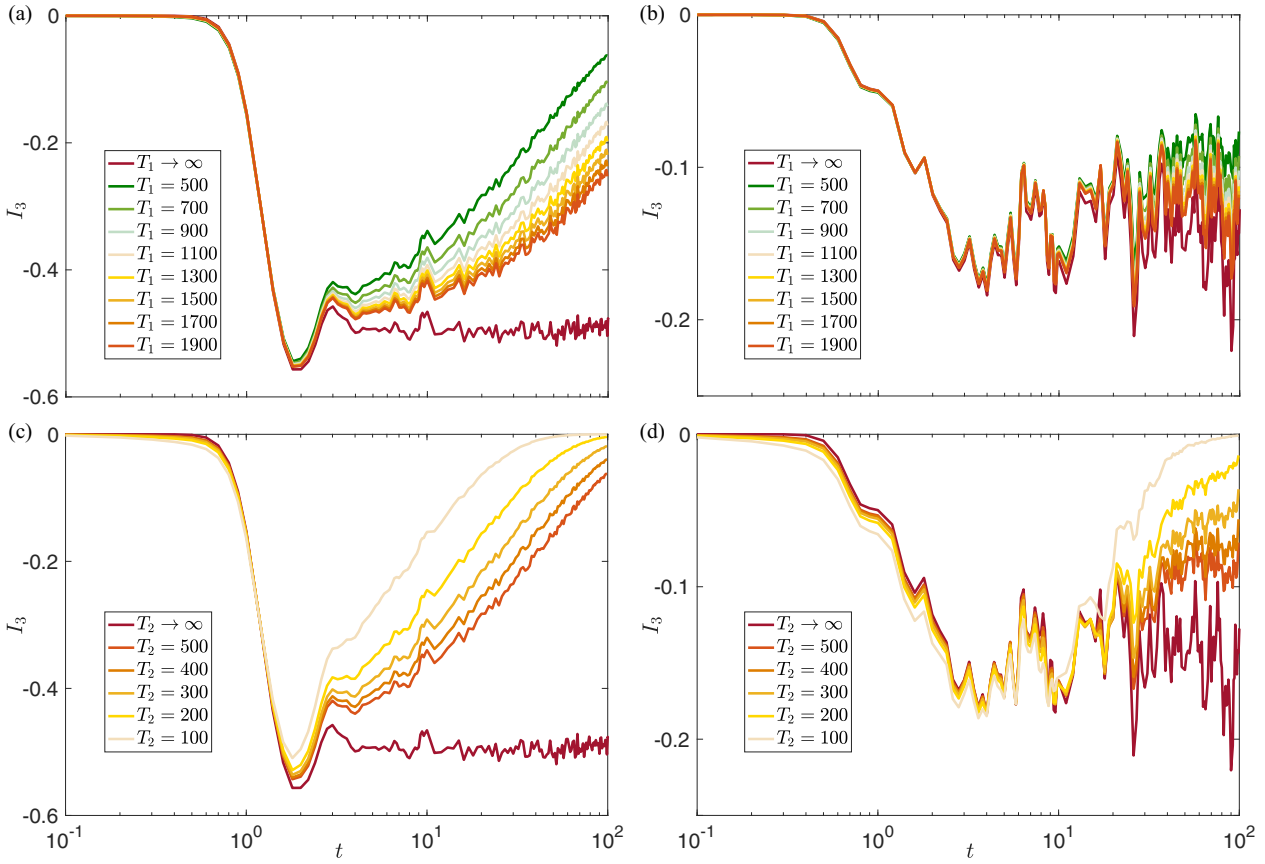

FIG. 6. The dynamics of the TMI I_3 for the superconducting circuit model [Eq. (8)] with various T_1 and the initial state (a) $|\theta, \phi\rangle = |\pi/2, 1.369\pi\rangle$ and (b) $|\theta, \phi\rangle = |\pi/2, 0.369\pi\rangle$. The dynamics of the TMI I_3 with various T_2 and the initial state (c) $|\theta, \phi\rangle = |\pi/2, 1.369\pi\rangle$ and (d) $|\theta, \phi\rangle = |\pi/2, 0.369\pi\rangle$. The units of time t, T_1, and T_2 are $1/\lambda$.

Page value, while in the lower-DOS regime, the EE becomes smaller.

We have verified that the most efficient information scrambling, diagnosed by the TMI with a saturated value around -0.5, can be obtained from the Page value. In the strong-thermalization regime, the long-time quenched states can be approximate to a superposition of eigenstates with the Page value of EE. Consequently, large information scrambling corresponds to strong thermalization. The aforementioned physical argument can also support the claim that small information scrambling corresponds to weak thermalization.

IV. DISCUSSION

We have investigated the quantum information scrambling quantified by the TMI in the nonintegrable Ising model where both strong and weak thermalization exist. We reveal that

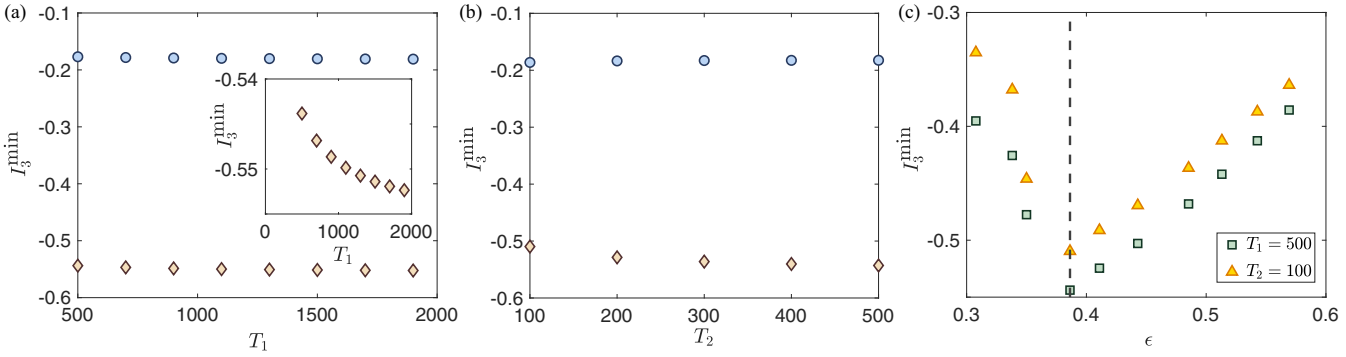

FIG. 7. The minimum of I_3 for the superconducting circuit model [Eq. (8)] with $t \leqslant 10$, i.e., $I_3^{\min}$, as a function of (a) T_1 and (b) T_2. The circle and diamond points in (a) and (b) refer to the results of weak and strong thermalization, i.e., with the initial state $|\theta, \phi\rangle = |\pi/2, 0.369\pi\rangle$ and $|\pi/2, 1.369\pi\rangle$, respectively. (c) The dependence of $I_3^{\min}$ on the normalization energy of initial states. The units of time t, T_1, and T_2 are $1/\lambda$.

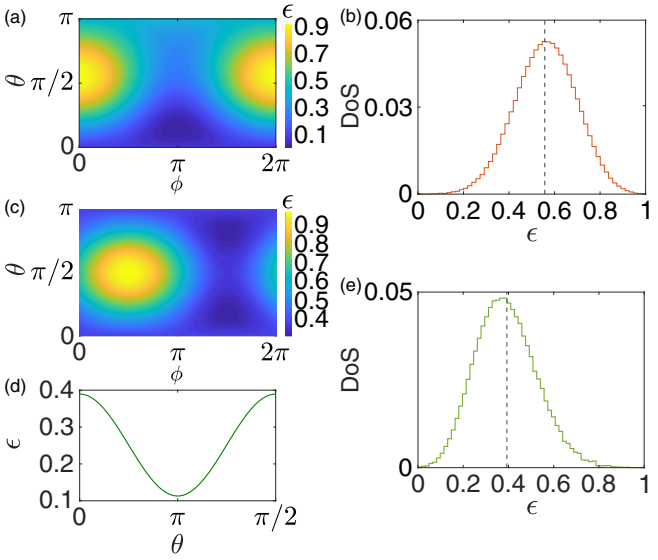

FIG. 8. (a) The normalized energy ϵ of isotropic initial states as a function of θ and ϕ in the nonintegrable Ising model [Eq. (5)]. (b) The DOS as a function of ϵ for the nonintegrable Ising model [Eq. (5)]. The dashed line highlights the normalized energy corresponding to the maximum DOS, $\epsilon \simeq 0.5602$. (c) The normalized energy ϵ of isotropic initial states as a function of θ and ϕ in the superconducting circuit model [Eq. (8)]. (d) The normalized energy ϵ of Néel-type initial states as a function of θ with $\phi = 0$ in the superconducting circuit model [Eq. (8)]. (e) The DOS as a function of ϵ for the superconducting circuit model [Eq. (8)]. The dashed line highlights the normalized energy corresponding to the maximum DOS, $\epsilon \simeq 0.3930$.

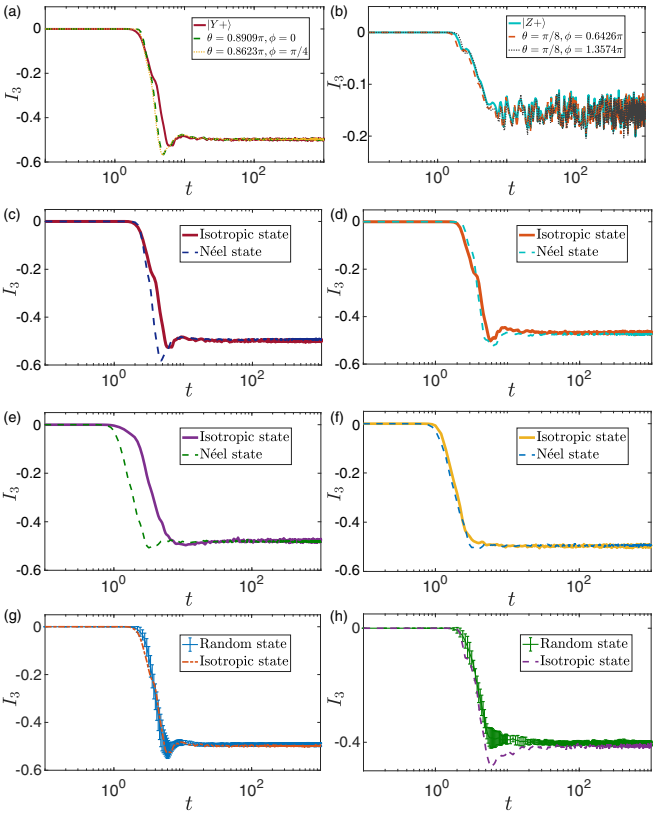

FIG. 9. (a) Time evolution of the TMI with different isotropic initial states with the same normalized energy $\epsilon = 0.5602$ in the nonintegrable Ising model [Eq. (5)]. The unit of time t is $1/J$. (b) Similar to (a) but with another $\epsilon = 0.0812$. (c) In the nonintegrable Ising model [Eq. (5)], the dynamics of TMI I_3 for the isotropic initial state $|Y+\rangle$ and the Néel-type initial state with $\theta = \pi/2$. The value of ϵ for both initial states is 0.5602. (d) Similar to (c), but for the isotropic initial state $|\theta = 0.5\pi, \phi = 0.4\pi\rangle$ and the Néel-type initial state with $\theta = 0.7013\pi$. The value of ϵ for both initial states is 0.6690. (e) In the superconducting circuit model [Eq. (8)], the dynamics of TMI I_3 for the isotropic initial state $|\theta = 0.18\pi, \phi = 1.5\pi\rangle$ and the Néel-type initial state with $\theta = 0.1810\pi$. The value of ϵ for both initial states is 0.3093. The unit of time t is $1/\lambda$. (f) Similar to (e), but for the isotropic initial state $|\theta = 0.4\pi, \phi = 1.5\pi\rangle$ and the Néel-type initial state with $\theta = 0.1124\pi$. The value of ϵ for both initial states is 0.3564. (g) In the nonintegrable Ising model [Eq. (5)], the dynamics of I_3 for the isotropic initial state $|\theta = 0.5\pi, \phi = 0.5\pi\rangle$ and ten randomly chosen states. The value of ϵ for all initial states is 0.5602. The unit of time t is $1/J$. (h) Similar to (g) but for the isotropic initial states $|\theta = 0.3\pi, \phi = 0.5\pi\rangle$ and ten randomly chosen states. The value of ϵ for all initial states is 0.3541.

the efficient and slow information scrambling occurs in the regime of strong and weak thermalization, respectively. Taking the recent developments of quantum simulations based on the one-dimensional array of superconducting qubits [22,25], we present an experimental protocol to realize a nonintegrable model and observe strong and weak thermalization in this platform. We have also calculated the TMI in the superconducting qubit chain, and shown that the relation between the TMI and the degree of thermalization revealed in the nonintegrable Ising model can be demonstrated in superconducting qubits, even with decoherence effects.

Reference [32] has revealed the weak and strong thermalization in the long-range Ising model which describes the trapped-ion quantum simulator [44]. As a consequence, this work may inspire the investigations on the TMI in long-range interacting systems [45,46], especially in the presence of weak and strong thermalization [32]. Besides the weak thermalization, the weak ergodicity breaking characterized by the long-lived oscillations can also be originated from quantum many-body scars [47,48], and the study of information scrambling with quantum many-body scars is another intriguing direction to explore in the future.

Quantum thermalization dynamics has been experimentally studied in optical lattice [49] and trapped ions [50]. Previous experiments mainly focused on the strong thermalization (which is actually regarded as the conventional quantum thermalization), and a distinct comparison between strong and weak thermalization remains absent. Our proposed scheme to probe strong and weak thermalization can enlighten experimental observation of the phenomena using the analog quantum simulation.

It has been shown that the normalized energy plays a key role in the MBL mobility edge [51–54]. The relation between information scrambling and normalized energy revealed by our work could provide new insight into the mobility edge. Furthermore, the slow information scrambling in the weak-thermalization region has potential applications

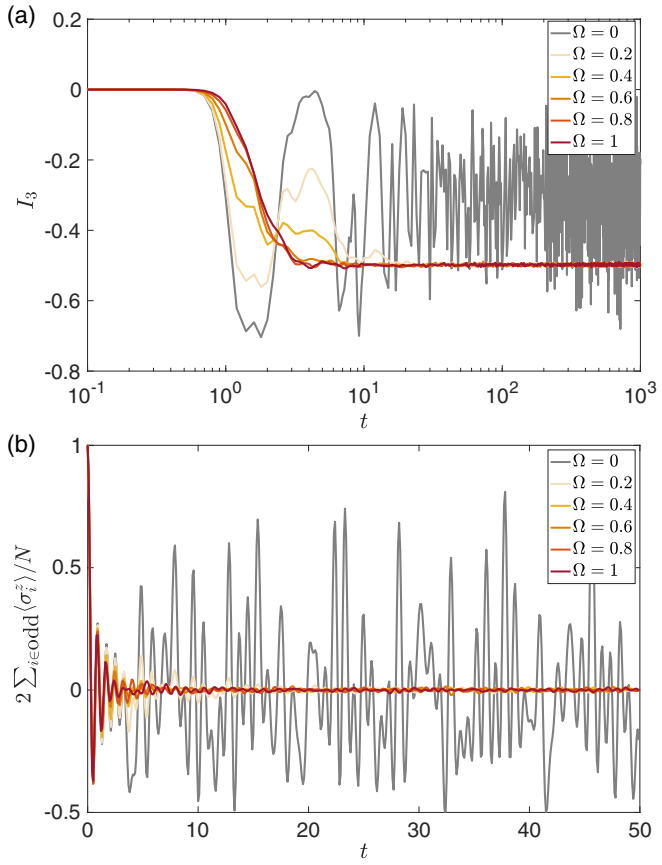

FIG. 10. (a) Time evolution of the TMI for the Hamiltonian $H_{XY} + H_{\text{drive}}$ with $\lambda = 1$, and several values of Ω. (b) Similar to (a) but for the local observable $\frac{2}{N}\sum_{i\in\text{odd}}\sigma_i^z$. The unit of time t is $1/\lambda$.

for quantum information storage devices [25] and stabilizing out-of-equilibrium phases of matter [55,56].

ACKNOWLEDGMENTS

We acknowledge the enlightening discussion with M. C. Bañuls and Q. Tang. This work was supported by National Key R&D Program of China (Grants No. 2016YFA0302104 and No. 2016YFA0300600), National Natural Science Foundation of China (Grants No. 11904018, No. 11774406, and No. 11934018), Strategic Priority Research Program of Chinese Academy of Sciences (Grant No. XDB28000000), and Beijing Natural Science Foundation (Grant No. Z200009).

APPENDIX A: ADDITIONAL RESULTS

Here, we present several additional results supporting the main text. For the nonintegrable Ising model [Eq. (5)], we plot the normalized energy of isotropic initial states $|\theta, \phi, +\rangle$, defined as $\epsilon(\theta, \phi) \equiv (\langle\theta, \phi, +|H_{\text{Ising}}|\theta, \phi, +\rangle - E_{\text{min}})/(E_{\text{max}} - E_{\text{min}})$ in the θ-ϕ plane in Fig. 8(a), and the DOS as a function of ϵ in Fig. 8(b). Similarly, for the system in Eq. (8) with $\lambda = \Omega = 1$, the normalized energy of isotropic initial states $|\theta, \phi, +\rangle$ is displayed in Fig. 8(c), showing that the normalized energy $\epsilon < 0.3093$ is not attainable for isotropic initial states. Thus, we consider another type of initial states, i.e., the Néel-type initial states

$$|\psi_0\rangle = |\Phi\rangle_{A1} \otimes |\theta_2, \phi_2, -\rangle \otimes |\theta_3, \phi_3, +\rangle \otimes \cdots \otimes |\theta_{N-1}, \phi_{N-1}, +\rangle \otimes |\theta_N, \phi_N, -\rangle \quad \text{(A1)}$$

with $\theta_i = \theta$, $\phi_i = \phi$ $(i = 1, 2, \ldots, N)$ and the number of qubits N as an even number for convenience. We further calculate the normalized energy of the Néel-type initial states with $\phi = 0$ and several values of θ. As shown in Fig. 8(d), the dynamics of TMI for the initial states with $\epsilon < 0.3093$ are available by choosing the Néel-type initial states. The DOS as a function of ϵ for the system in Eq. (8) with $\lambda = \Omega = 1$ is displayed in Fig. 8(f).

The results in Figs. 9(a) and 9(b) have suggested that for the isotropic state, the saturated value of TMI is directly dependent on the ϵ. Therefore, it can be predicted that the saturated value of TMI is insensitive to the specific initial states, i.e., the isotropic or Néel-type states, if the ϵ of the states are equal to each other. The results in Figs. 9(c)–9(f) provide further evidence for this prediction.

To demonstrate the relation between TMI and the ϵ of initial states in a more general case, we consider a type of initial states defined in Eq. (4) with θ_j (ϕ_j) randomly drawn from a uniform distribution $[0, \pi]$ ($[0, 2\pi]$), which are known as random initial states. We chose ten random initial states with $\epsilon \simeq 0.5602$, and plotted the time evolution of TMI in Fig. 9(g), in comparison with the TMI for the isotropic initial state $|\theta = 0.5\pi, \phi = 0.5\pi\rangle$. It is shown that the saturated values of TMI for isotropic and random initial states with identical ϵ are almost equal to each other. The claim is further verified for the normalized energy $\epsilon \simeq 0.3541$ [see Fig. 9(h)]. The error bars in Figs. 9(g) and 9(h) represent the standard deviations over random initial states.

APPENDIX B: REALIZATION OF HAMILTONIAN (8) IN A SUPERCONDUCTING QUBIT CHAIN

Conventionally, the Hamiltonian of a transmon qubit array can be described by the Bose-Hubbard model [22,25],

$$H_{\text{BH}} = \Lambda \sum_{i=1}^{N-1}(a_i^\dagger a_{i+1} + a_i a_{i+1}^\dagger) + \frac{U}{2}\sum_{i=1}^{N} n_i(n_i - 1), \quad \text{(B1)}$$

where $a_i^\dagger$ (a_i) is the bosonic creation (annihilation) operator, $n_i = a_i^\dagger a_i$, U is the strength of nonlinear interaction, and Λ refers to the nearest hopping strength. In the limit $U/\Lambda \to \infty$, Hamiltonian (B2) reduces to an XY model [57,58],

$$H_{XY} = \Lambda \sum_{i=1}^{N-1}(\sigma_i^+\sigma_{i+1}^- + \sigma_i^-\sigma_{i+1}^+) = \lambda \sum_{i=1}^{N-1}\left(\sigma_i^x\sigma_{i+1}^x + \sigma_i^y\sigma_{i+1}^y\right), \quad \text{(B2)}$$

with $\lambda = \Lambda/2$.

Actually, the nonequilibrium properties of the Bose-Hubbard model (B2) are close to those of the XY model (B2) when $U/\Lambda \gtrsim 8$ [58]. For the device in Ref. [22], $U/\Lambda \simeq 18$,

and the XY model can be experimentally studied using analog quantum simulation.

When the microwave drives with amplitude Ω are applied to each qubit, we can obtain [41]

$$H_{\text{drive}} = \Omega \sum_{j=1}^{N} e^{-i\varphi_j}\sigma_j^+ + e^{i\varphi_j}\sigma_j^-. \tag{B3}$$

By adjusting the phase of the microwave drives, one can force $\varphi = \varphi_j = \pi/2$ $(j = 1, 2, \ldots, N)$, and then H_{drive} can be rewritten as $H_{\text{drive}} = \Omega \sum_{j=1}^{N} \sigma_j^y$. Thus, Hamiltonian (8), i.e., $H_{\text{SQA}} = H_{XY} + H_{\text{drive}}$, can be realized in a qubit array.

To better understand the strong thermalization in system (8), we can rewrite the Hamiltonian in the σ^x basis:

$$\begin{aligned} H_{\text{SQP}} &= \Lambda \sum_{i=1}^{N-1} \sigma_i^z \sigma_{i+1}^z + \Omega \sum_{i=1}^{N} \sigma_i^x + \Omega \sum_{i=1}^{N-1} \sigma_i^x \sigma_{i+1}^x \\ &= H_0 + H_{\text{int.}}. \end{aligned} \tag{B4}$$

By employing the Jordan-Wigner transformation $\sigma_i^x = 1 - 2c_i^\dagger c_i$ and $\sigma_i^z = -\prod_{l<i}(1 - 2c_l^\dagger c_l)(c_i + c_i^\dagger)$ with $c_i^\dagger$ (c_i) referring to the fermionic creation (annihilation) operator, one can see that in Hamiltonian (B4), $H_0 \equiv \Lambda \sum_{i=1}^{N-1} \sigma_i^z \sigma_{i+1}^z + \Omega \sum_{i=1}^{N} \sigma_i^x$ as the Ising model without parallel field can be mapped to a quadratic system (free fermions). Moreover, the $H_{\text{int.}} \equiv \Omega \sum_{i=1}^{N-1} \sigma_i^x \sigma_{i+1}^x$ gives the Heisenberg coupling $c_i c_i c_{i+1} c_{i+1}$, from which the quantum thermalization and MBL are originated [59]. Based on above discussions, we explain the occurrence of the strong thermalization in the superconducting qubit array.

To illustrate the integrability breaking due to Eq. (B3), we calculate the dynamics of TMI with different values of Ω. Here, we consider a Néel-type initial state, i.e., Eq. (A1) with $\theta = 0$. There are two reasons behind the choice of the initial state. First, when $\Omega = 0$, the system H_{XY} has a conservation of the spin number $\sum_{i=1}^{N} \sigma_{i=1}^z$. The Néel-type initial state allows us to study the nonequilibrium dynamics of H_{XY} in the largest subspace. Second, for all $\Omega \geqslant 0$, the inverse temperature of the initial state is $\beta = 0$, and we can explore the breakdown of integrability because of H_{drive} without the influence of the degree of thermalization.

As shown in Fig. 10(a), in the integrable limit $\Omega = 0$, the TMI exhibits a dramatic oscillation and a recurrence of zero value during its dynamics. In contrast, with a finite value of Ω, the TMI tends to a stable negative value. Additionally, we also calculate the quench dynamics of the local observable $\mathcal{O} = \frac{2}{N} \sum_{i\in\text{odd}} \sigma_i^z$ to explore the integrability breaking and thermalization in the system. If thermalization occurs, the local observable converges to its thermal value [here the thermal value is $\langle\mathcal{O}\rangle_{\text{th}} = \text{Tr}(\mathcal{O}\rho_\beta) = 0$ since $\beta = 0$] [60]. In Fig. 10(b), we observe the convergence for nonzero Ω, while the strong oscillation of local observable in the integrable system with $\Omega = 0$ suggests the absence of thermalization in the integrable model H_{XY}.

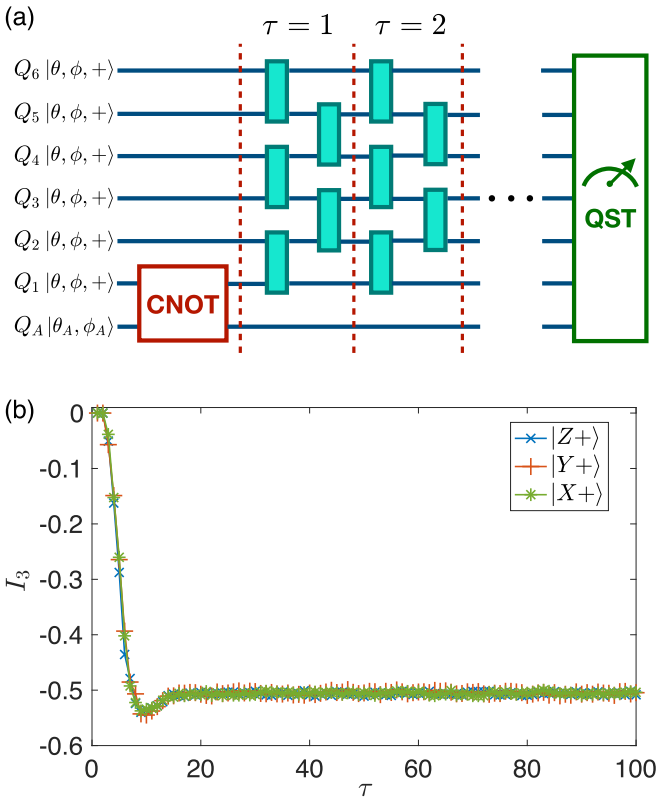

FIG. 11. (a) Schematic representation of the random circuit model with the system size $N = 6$. Each two-site gate is a 4×4 unitary matrix, which is randomly chosen from the Haar distribution. (b) The dynamics of the TMI for the Haar random circuit with $N = 14$, and three different initial states $|Z+\rangle$, $|X+\rangle$, and $|Y+\rangle$.

APPENDIX C: TRIPARTITE MUTUAL INFORMATION IN A HAAR RANDOM CIRCUIT

Here, we numerically show that the TMI approaches a value around -0.5 at long time if the dynamics is coming from a Haar random circuit. In Fig. 11(a), we plot the structure of the Haar random circuit comprised of two-qubit gates, which has been widely employed to study thermalization and scrambling [61]. The dynamics of TMI with three initial states $|Z+\rangle$, $|X+\rangle$, and $|Y+\rangle$ is displayed in Fig. 11(b), suggesting that the convergence of TMI to -0.5 is independent of the choice of initial states. Since for the Haar random circuit the temperature and normalized energy of initial states are not well defined, the slow information scrambling in the presence of weak thermalization cannot be observed in the random circuit system.

APPENDIX D: ENTANGLEMENT ENTROPY OF EIGENSTATES AND THE SUPERPOSITION OF QUENCHED STATES

In this Appendix, we present the numerical results relevant to the physical argument that explains the relation between the TMI and the normalized energy of initial states.

We calculate the half-chain EE defined as $S(\rho_A) = -\text{Tr}(\rho_A \ln \rho_A)$, for all eigenstates of the nonintegrable Ising model [Eq. (5)] and the superconducting circuit model

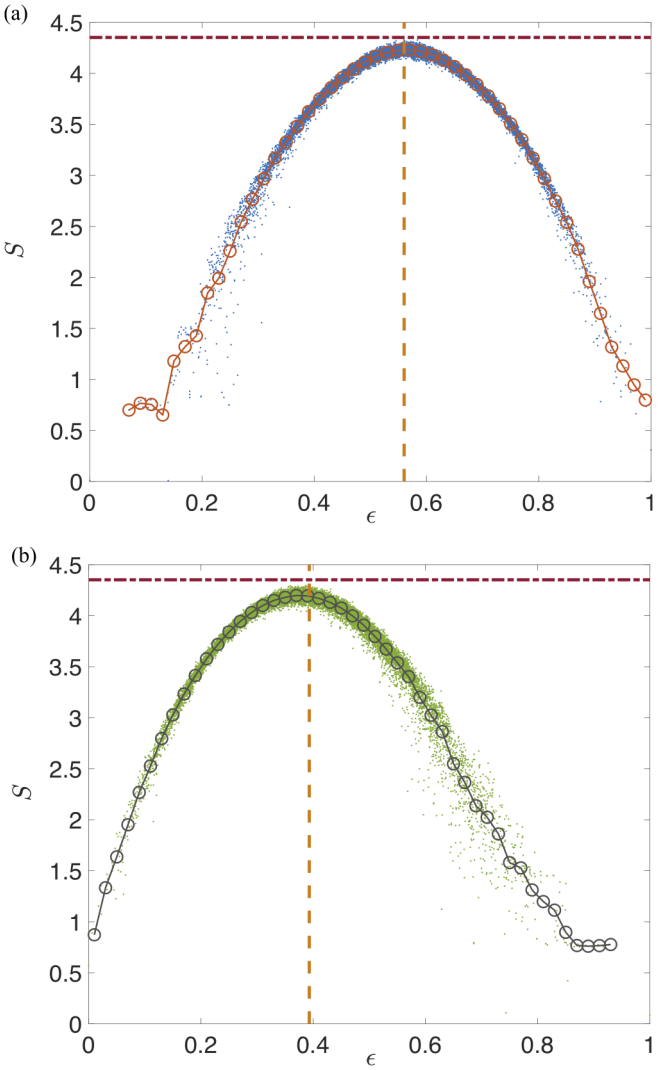

FIG. 12. (a) The half-chain EE for the eigenstates of the nonintegrable Ising model [Eq. (5)]. The dots present the EE of a single eigenstate with the normalized energy ϵ, and the circles present the averaged EE as a function of ϵ with an energy window $\epsilon \pm 0.01$. (b) Similar to (a) but for the superconducting circuit model [Eq. (8)]. The horizontal line in (a) and (b) represents the Page value of the EE, $S^{\text{Page}} \simeq 4.352$. The vertical lines in (a) and (b) represent the ϵ with maximum DOS [see also the vertical lines in Figs. 8(b) and 8(e)].

[Eq. (8)]. The system size is $N = 14$, and the ρ_A is the RDM of the subsystem consisting of the qubits $Q_1, Q_2, \ldots, Q_7$. The

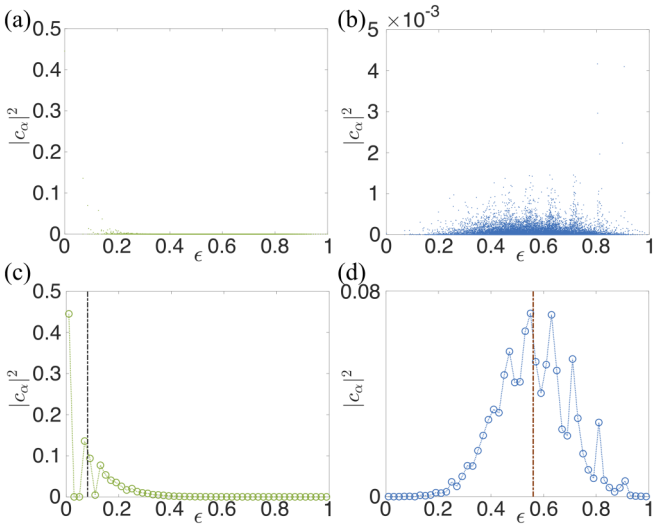

FIG. 13. (a) For the quenched state $|\psi_t\rangle = \exp(-iHt)|\psi_0\rangle$ with $t = 1000$, H being the Hamiltonian of the nonintegrable Ising model [Eq. (5)], and the initial state $|\psi_0\rangle = |Z+\rangle$ in the regime of weak thermalization, the parameter $|c_\alpha|^2$ of all the eigenstates as a function of the normalized energy ϵ. (b) Similar to (a) but for the initial state $|\psi_0\rangle = |Y+\rangle$ in the regime of strong thermalization. (c) Similar to (a) but for the sum of $|c_\alpha|^2$ as a function of the normalized energy ϵ with an energy window $\epsilon \pm 0.01$. (d) Similar to (c), but for the data of $|c_\alpha|^2$ in (b). The vertical lines in (c) and (d) refer to $\epsilon = 0.0812$ and $\epsilon = 0.5602$, being the normalized energy of the initial state $|Z+\rangle$ and $|Y+\rangle$, respectively.

results are displayed in Fig. 12. One can see that the shape of EE as a function of eigenstates' normalized energy ϵ is similar to the DOS plotted in Figs. 8(b) and 8(e).

In addition, we focus on the quenched state $|\psi_t\rangle = \exp(-iHt)|\psi_0\rangle$, where $t = 1000$, H is the Hamiltonian of the nonintegrable Ising model [Eq. (5)], and $|\psi_0\rangle$ is the initial state. The quenched state can be written as $|\psi_t\rangle = \sum_\alpha c_\alpha |E_\alpha\rangle$, where $|E_\alpha\rangle$ is the αth eigenstate of H, and $|c_\alpha|^2 = |\langle E_\alpha|\psi_t\rangle|^2$. With the initial state $|Z+\rangle$ in the weak-thermalization regime, we plot the parameter $|c_\alpha|^2$ as a function of the normalized energy ϵ of the eigenstate $|E_\alpha\rangle$ in Fig. 13(a), and plot the sum of $|c_\alpha|^2$ in an energy window $\epsilon \pm 0.01$ in Fig. 13(c). It is shown that the $|c_\alpha|^2$ is large for the eigenstates near the ground state. The results of $|c_\alpha|^2$ for another initial state $|Y+\rangle$ are displayed in Figs. 13(b) and 13(d), suggesting that the maximum value of $|c_\alpha|^2$ can be achieved for the eigenstates whose ϵ is close to 0.5602, being the ϵ of initial state $|Y+\rangle$.

[1] R. J. Lewis-Swan, A. Safavi-Naini, A. M. Kaufman, and A. M. Rey, Nat. Rev. Phys. **1**, 627 (2019).

[2] J. Eisert, M. Friesdorf, and C. Gogolin, Nat. Phys. **11**, 124 (2015).

[3] P. Hayden and J. Preskill, J. High Energy Phys. 09 (2007) 120.

[4] Y. Sekino and L. Susskind, J. High Energy Phys. 10 (2008) 065.

[5] J. Maldacena, S. H. Shenker, and D. Stanford, J. High Energy Phys. 08 (2016) 106.

[6] P. Hosur, X.-L. Qi, D. A. Roberts, and B. Yoshida, J. High Energy Phys. 02 (2016) 004.

[7] C. Sünderhauf, L. Piroli, X.-L. Qi, N. Schuch, and J. I. Cirac, J. High Energy Phys. 11 (2019) 038.

[8] Y. O. Nakagawa, G. Sárosi, and T. Ugajin, J. High Energy Phys. 07 (2018) 002.

[9] K. A. Landsman, C. Figgatt, T. Schuster, N. M. Linke, B. Yoshida, N. Y. Yao, and C. Monroe, Nature (London) **567**, 61 (2019).

[10] B. Swingle, Nat. Phys. **14**, 988 (2018).

[11] D. J. Luitz and Y. Bar Lev, Phys. Rev. B **96**, 020406(R) (2017).

[12] Y. Huang, Y.-L. Zhang, and X. Chen, Ann. Phys. **529**, 1600318 (2017).
[13] R.-Q. He and Z.-Y. Lu, Phys. Rev. B **95**, 054201 (2017).
[14] S. Sahu, S. Xu, and B. Swingle, Phys. Rev. Lett. **123**, 165902 (2019).
[15] X. Chen, T. Zhou, D. A. Huse, and E. Fradkin, Ann. Phys. **529**, 1600332 (2017).
[16] Z.-H. Sun, J.-Q. Cai, Q.-C. Tang, Y. Hu, and H. Fan, Ann. Phys. **532**, 1900270 (2020).
[17] H. Shen, P. Zhang, R. Fan, and H. Zhai, Phys. Rev. B **96**, 054503 (2017).
[18] C. B. Dağ, K. Sun, and L.-M. Duan, Phys. Rev. Lett. **123**, 140602 (2019).
[19] B.-B. Wei, G. Sun, and M.-J. Hwang, Phys. Rev. B **100**, 195107 (2019).
[20] M. Gärttner, J. G. Bohnet, A. Safavi-Naini, M. L. Wall, J. J. Bollinger, and A. M. Rey, Nat. Phys. **13**, 781 (2017).
[21] J. Li, R. Fan, H. Wang, B. Ye, B. Zeng, H. Zhai, X. Peng, and J. Du, Phys. Rev. X **7**, 031011 (2017).
[22] Z. Yan *et al.*, Science **364**, 753 (2019).
[23] P. Jurcevic *et al.*, Phys. Rev. Lett. **119**, 080501 (2017).
[24] K. Xu *et al.*, Phys. Rev. Lett. **120**, 050507 (2018).
[25] B. Chiaro *et al.*, arXiv:1910.06024.
[26] K. Li *et al.*, npj Quantum Inf. **5**, 30 (2019).
[27] E. Iyoda and T. Sagawa, Phys. Rev. A **97**, 042330 (2018).
[28] O. Schnaack, N. Bölter, S. Paeckel, S. R. Manmana, S. Kehrein, and M. Schmitt, Phys. Rev. B **100**, 224302 (2019).
[29] M. C. Bañuls, J. I. Cirac, and M. B. Hastings, Phys. Rev. Lett. **106**, 050405 (2011).
[30] M. B. Hastings and R. Mahajan, Phys. Rev. A **91**, 032306 (2015).
[31] C.-J. Lin and O. I. Motrunich, Phys. Rev. A **95**, 023621 (2017).
[32] F. Liu, R. Lundgren, P. Titum, G. Pagano, J. Zhang, C. Monroe, and A. V. Gorshkov, Phys. Rev. Lett. **122**, 150601 (2019).
[33] U. L. Heras, A. Mezzacapo, L. Lamata, S. Filipp, A. Wallraff, and E. Solano, Phys. Rev. Lett. **112**, 200501 (2014).
[34] Y. Salathé *et al.*, Phys. Rev. X **5**, 021027 (2015).
[35] G. Wendin, Rep. Prog. Phys. **80**, 106001 (2017).
[36] D. Ristè, S. Poletto, M.-Z. Huang, A. Bruno, V. Vesterinen, O.-P. Saira, and L. DiCarlo, Nat. Commun. **6**, 6983 (2015).
[37] Y. Chen, C. Neill, P. Roushan, N. Leung, M. Fang, R. Barends, J. Kelly, B. Campbell, Z. Chen, B. Chiaro, A. Dunsworth, E. Jeffrey, A. Megrant, J. Y. Mutus, P. J. J. O'Malley, C. M. Quintana, D. Sank, A. Vainsencher, J. Wenner, T. C. White, M. R. Geller, A. N. Cleland, and J. M. Martinis, Phys. Rev. Lett. **113**, 220502 (2014).
[38] E. Lieb, T. Schultz, and D. Mattis, Ann. Phys. **16**, 407 (1961).
[39] M. Rigol, V. Dunjko, V. Yurovsky, and M. Olshanii, Phys. Rev. Lett. **98**, 050405 (2007).
[40] G. Biroli, C. Kollath, and A. M. Läuchli, Phys. Rev. Lett. **105**, 250401 (2010).
[41] K. Xu *et al.*, Sci. Adv. **6**, eaba4935 (2020).
[42] D. N. Page, Phys. Rev. Lett. **71**, 1291 (1993).
[43] J. Johansson, P. Nation, and F. Nori, Comput. Phys. Commun. **183**, 1760 (2012).
[44] C. Monroe *et al.*, Rev. Mod. Phys. **93**, 025001 (2021).
[45] S. Pappalardi, A. Russomanno, B. Žunkovič, F. Iemini, A. Silva, and R. Fazio, Phys. Rev. B **98**, 134303 (2018).
[46] S. P. Kelly, E. Timmermans, and S.-W. Tsai, Phys. Rev. A **102**, 052210 (2020).
[47] H. Bernien *et al.*, Nature (London) **551**, 579 (2017).
[48] C. J. Turner, A. A. Michailidis, D. A. Abanin, M. Serbyn, and Z. Papić, Nat. Phys. **14**, 745 (2018).
[49] A. M. Kaufman *et al.*, Science **353**, 794 (2016).
[50] B. Neyenhuis *et al.*, Sci. Adv. **3**, e1700672 (2017).
[51] D. J. Luitz, N. Laflorencie, and F. Alet, Phys. Rev. B **91**, 081103(R) (2015).
[52] T. B. Wahl, A. Pal, and S. H. Simon, Nat. Phys. **15**, 164 (2019).
[53] E. Altman, Nat. Phys. **14**, 979 (2018).
[54] Q. Guo *et al.*, Nat. Phys. **17**, 234 (2021).
[55] A. C. Potter, T. Morimoto, and A. Vishwanath, Phys. Rev. X **6**, 041001 (2016).
[56] D. V. Else, C. Monroe, C. Nayak, and N. Y. Yao, Annu. Rev. Condens. Matter Phys. **11**, 467 (2020).
[57] M. A. Cazalilla, R. Citro, T. Giamarchi, E. Orignac, and M. Rigol, Rev. Mod. Phys. **83**, 1405 (2011).
[58] M. Cramer, A. Flesch, I. P. McCulloch, U. Schollwöck, and J. Eisert, Phys. Rev. Lett. **101**, 063001 (2008).
[59] J. H. Bardarson, F. Pollmann, and J. E. Moore, Phys. Rev. Lett. **109**, 017202 (2012).
[60] R. Nandkishore and D. A. Huse, Annu. Rev. Condens. Matter Phys. **6**, 15 (2015).
[61] C. W. von Keyserlingk, T. Rakovszky, F. Pollmann, and S. L. Sondhi, Phys. Rev. X **8**, 021013 (2018).